Nano Energy 72 (2020) 104698

Contents lists available at ScienceDirect

Nano Energy

journal homepage: http://www.elsevier.com/locate/nanoen

Full paper

Synchronized enhancement of thermoelectric properties of higher manganese silicide by introducing Fe and Co nanoparticles

Gwansik Kim [a,1], Hyun-Sik Kim [b,1], Ho Seong Lee [c], Jeongmin Kim [d], Kyu Hyoung Lee [a], Jong Wook Roh [e,**], Wooyoung Lee [a,*]

[a] Department of Materials Science and Engineering, Yonsei University, Seoul, 03722, Republic of Korea
[b] Department of Materials Science and Engineering, Hongik University, Seoul, 04066, Republic of Korea
[c] School of Materials Science and Engineering, Kyungpook National University, 80 Daehak-ro, Buk-gu, Daegu, 41566, Republic of Korea
[d] DGIST, 333 Techno Jungang-daero, Hyeonpung-eup, Dalseong-gun, Daegu, 42988, Republic of Korea
[e] School of Nano & Materials Science and Engineering, Kyungpook National University, Gyeongsangbuk-do, 37224, Republic of Korea

ARTICLE INFO

Keywords:
Nanocomposite
Thermoelectric
Higher manganese silicide
Nanometal decoration
Energy filtering effect

ABSTRACT

Introduction of nanophases is known to be effective in improving thermoelectric performance as it allows the simultaneous engineering of electronic and thermal transports. In this study, we synthesized Fe and Co nanoparticle-embedded $MnSi_{1.787}Al_{0.01}$ nanocomposites through a simple nanometal-decoration technique and spark plasma sintering. The nanoparticles introduced in the matrix caused energy band bending at the matrix–nanoparticle interface, which induced charge transfer and energy filtering effects. These two seemingly opposing effects were combined so as to increase the power factor of the nanocomposites by enhancing the electronic transport. Moreover, we found that the lattice thermal conductivity decreased owing to intensified phonon scattering. Hence, a maximum *ZT* of 0.53 (at 773 K) was achieved in 0 .6 vol% Fe nanoparticle-embedded nanocomposites, which is 25% higher than that of the pristine sample.

1. Introduction

Over the past few decades, thermoelectric energy conversion materials have received considerable attention as promising candidates for power generation and cooling application [1]. Specifically, mid-to-high-temperature thermoelectric (TE) materials such as PbTe-, Skutterudites-, half-Heusler-, SnSe-, and silicide-based TE materials have been studied extensively for industrial applications such as electronic vehicles and waste heat recovery [2–7]. In this respect, silicide-based TE materials have numerous advantages over other mid-to-high temperature TE materials; these include non-toxicity, abundance, and competitive prices. Among silicide-based TE materials, higher manganese silicide (HMS) is typically known as an ideal *p*-type counterpart for *n*-type Mg_2Si owing to their comparable thermal expansion coefficients (Mg_2Si: 13.0 × 10^{-6} K^{-1}, $Mg_2Si_{1-x}Sn_x$: 17.0 × 10^{-6} K^{-1}, and HMS 11.0–13.0 × 10^{-6} K^{-1}) that must be considered in TE module fabrication [8–10]. HMSs are more environment friendly and cheaper than other candidates (HMS: 1.5 US$/kg and Mg_2Si: 5.4 US $/kg) [11]. Moreover, they offer advantages such as high thermal stability, mechanical reliability (~1.63 MPa $m^{1/2}$), high Seebeck coefficient (*S*, 130–220 $\mu V\ K^{-1}$), and moderate electrical conductivity (σ, 70, 000–30,000 S m^{-1}) [12,13]. Despite these advantages, the intrinsically high thermal conductivity of HMS (3.0 ± 0.2 W m^{-1} K^{-1} at 773 K) has been a significant obstacle in the utilization of HMSs in modules. Many attempts have been made to suppress the thermal conductivity without deteriorating the electronic transport properties. Itoh et al. reported that TE properties were slightly enhanced due to the reduced thermal conductivity by Fe doping [14]. Luo et al. demonstrated that micro-scale MnSi metallic phases in HMS matrix that were formed using a melt-spinning process are effective in reducing the lattice thermal conductivity (κ_{lat}) [15]. Sleemi et al. reported that the introduction of ytterbium inclusions lowered the thermal conductivity, thereby leading to the enhancement of *ZT* in Yb-HMS nanocomposites [16]. These studies revealed that the doping effect and the introduction of nanophases is effective in reducing the κ_{lat}, whereas the increase in power factor is limited owing to the reduction in carrier mobility (μ_{Hall}) and

* Corresponding author.
** Corresponding author.
E-mail addresses: jw.roh@knu.ac.kr (J.W. Roh), wooyoung@yonsei.ac.kr (W. Lee).
[1] These authors contributed equally.

https://doi.org/10.1016/j.nanoen.2020.104698
Received 3 December 2019; Received in revised form 20 February 2020; Accepted 10 March 2020
Available online 13 March 2020

difficulties in band engineering [17]. This means that precisely defined nanophases are required in order to simultaneously manipulate the electronic and thermal transport properties. Apart from these efforts, the increasing power factor have been challenging issue in HMS based TE materials. Barczak et al. reported on the high power factor by co-doping of Fe and Al in $Mn_{0.9}Fe_{0.1}Si_{1.65}Al_{0.1}$ [18]. Recently, a study was conducted to improve the TE properties of $Ba_{0.3}In_{0.3}Co_4Sb_{12}$ by introducing soft-magnet transition-metal nanoparticles (NPs) [19]. The power factor of the magnetic NP-embedded nanocomposites significantly increased owing to the carrier transfer (high carrier concentration (n_H)) and energy filtering effects (high S) that were induced by multiple scattering from the superparamagnetic magnetic NPs. The κ_{lat} values of the nanocomposites were reduced by the intensified phonon scattering due to the randomly turned magnetic domain for superparamagnetic NPs. This result suggested a new approach that allows the simultaneous manipulation of electron and phonon transport.

In the present study, we synthesized bulk nanocomposites of $MnSi_{1.787}Al_{0.01}$ with soft-magnet transition-metal (Fe and Co) NPs using a nanometal decoration technique and spark plasma sintering (SPS) to simultaneously control the electronic and thermal transport properties. Fe and Co were selected as the NPs because the proper work function and magnetic properties of Fe and Co are effective for implementing band structure engineering and reducing κ_{lat}. The power factor of the nanocomposites was enhanced by well-controlled band alignment. Additionally, the κ_{lat} was slightly reduced by intensified phonon scattering owing to the increased interface density and randomly turned magnetic domain. The maximum ZT value was estimated to be 0.53 at 773 K, which corresponds to a 25% increase in comparison with that in the case of pristine samples.

2. Material and methods

2.1. Synthesis of materials

Al-doped HMS ($MnSi_{1.787}Al_{0.01}$) polycrystalline powders were synthesized by a conventional solid-state reaction. Based on our previous work [20], Al-doped HMS has higher TE properties than un-doped HMS. In order to maximize TE properties by the introduction of Fe and Co NPs, Al-doped HMS were used as matrix materials. High purity elements Mn (99.95%, Alfa Aesar), Si (99.9%, Alfa Aesar), and Al (99.5%, Alf Aesar) were weighed according to their stoichiometric compositions and ground for 30 min using an agate mortar. The mixed powders (50 g) were placed in vacuum-sealed quartz tubes before a solid-state reaction process. The vacuum-sealed quartz tubes were annealed at 1323 K for 48 h to fabricate homogeneous $MnSi_{1.787}Al_{0.01}$ ingots. The ingots were crushed into powders using a high-energy ball mill. Next, $MnSi_{1.787}Al_{0.01}$ powders were put through a sieve with a mesh size of 53 μm. For the decoration of NPs (Fe and Co) onto the surface of $MnSi_{1.787}Al_{0.01}$ powders, each metal acetate (iron (II) acetate, $(CH_3COO)_2Fe$ and cobalt (II) acetate, $(CH_3COO)_2Co$) were mixed with the sieved $MnSi_{1.787}Al_{0.01}$ powders for 5 min in an Ar atmosphere (to prevent the oxidation of samples) using a high-energy ball milling system (8000D, SPEX, USA). Then, the hybrid powders of metal acetate and $MnSi_{1.787}Al_{0.01}$ powders were annealed at 573 K for 2 h in a mixed gas atmosphere (95% N_2 and 5% H_2) to remove the acetate (–CH_3COO–) from the metal acetates.

2.2. Characterization of thermal and electrical properties

To measure the TE properties, the reduced hybrid powders were densified by SPS under a vacuum of $\sim 10^{-3}$ torr. In this study, the temperature, pressure, and time for SPS were maintained at 1193 K, 60 MPa, and 5 min, respectively, which were the optimized conditions for the sintering of HMS according to our previous study [21]. After the sintering process, the relative densities of the samples were estimated to be in the range of 90–95% of the theoretical density. The sintered pellets were cut and polished into disc-type samples for measuring their TE properties. The temperature dependences of σ and S of the nanocomposites were evaluated using a ZEM-3 (Ulvac, Japan) between 300 and 873 K. The total thermal conductivity (κ_{tot}) values were calculated using the equation $\kappa_{tot} = \rho_s C_p \lambda$, where λ is thermal diffusivity, C_p is the specific heat capacity, and ρ_s is the density. The values of λ and C_p were measured using the laser flash method (Netszch LFA-457, Germany) and differential scanning calorimetry (DSC; DSC 8000, PerkinElmer, USA) under vacuum from 373 to 873 K.

Hall effect measurements were measured using a standard Hall effect measurement system (NanoMagnetics Instruments ezHEMS, UK). Hall effect measurements were carried out on the 0.6 × 0.6 cm samples in the van der Pauw configuration under a 1 T magnetic field and room temperature, and the n_H and μ_{Hall} were estimated using the one-band model without considering the minority carriers. The work functions of $MnSi_{1.787}Al_{0.01}$ and metal NPs (ϕ and ϕ_m, respectively) were determined by ultraviolet photoemission spectroscopy (UPS, ESCALAB 250Xi, Thermo Fisher, UK) with a He I radiation source ($h\nu = 21.2$ eV). The M (Magnetization)–H (Magnetic field) curves were measured using a vibrating sample magnetometer (VSM) at room temperature.

2.3. Microscopic analysis

Phase analysis was performed for each sample using X-ray diffraction (XRD; Ultima IV/ME 200DX, Rigaku, Japan) with CuKα radiation. SEM (JEOL-7800F, JEOL Ltd., Japan) was used to observe the microstructure of the hybrid powders (size and distribution of the NPs). High-resolution transmission electron microscopy (HRTEM) image, selected area electron diffraction (SAED) pattern, and energy dispersive spectrometry (EDS) images were obtained by Field Emission Transmission Electron Microscope (FE-TEM; Titan G2 ChemiSTEM Cs Probe, FEI Company, USA) to confirm the position and size of the NPs in the nanocomposites. For investigation of the chemical state and doping effect of Fe and Co in the nanocomposite, X-ray photoemission spectroscopy (XPS; K-alpha, Thermo Scientific Inc., UK) spectra of Mn and Si 2p core levels were recorded at a pass energy of 40 eV and step size of 0.1 eV.

2.4. Thermal conductivity calculation

κ_{tot} involves three different conduction mechanisms originating from (1) phonon vibrations (κ_{lat}), (2) transport of charged carriers (κ_{ele}), and (3) bipolar conduction (κ_{bp}). To accurately compute the κ_{bp} of pristine $MnSi_{1.787}Al_{0.01}$ and metal (Fe and Co) NP-embedded nanocomposites, much information of their conduction bands (CBs) and valence bands (VBs) must be available in the literature. Unfortunately, owing to a lack of previous studies on $MnSi_{1.787}Al_{0.01}$ composition, we could not utilize two-band modeling (1 CB and 1 VB) to calculate the theoretical κ_{bp}. Instead, we approximated κ_{bp} using the relation given below [22]. κ_{ele} was determined using the Wiedemann-Franz law ($\kappa_{ele} = L\sigma T$, where L is the Lorenz number). L was calculated by a single parabolic band (SPB) model under the acoustic phonon scattering assumption [23]. Lastly, κ_{lat} was estimated using the Debye-Callaway model. Details on κ_{lat} modeling are provided in the following section.

3. Results and discussion

3.1. Phase and microstructures of Fe and Co NP-embedded nanocomposites

We fabricated soft-magnet transition-metal (Fe and Co) NP-embedded nanocomposites and investigated the effect of the soft-magnet transition-metal NPs on the TE properties and the microstructure. Typically, the introduction of nanophases is a traditional strategy used to improve TE properties by controlling electronic or thermal transport properties. For improving TE properties, it is necessary to manipulate the electronic and thermal transport properties

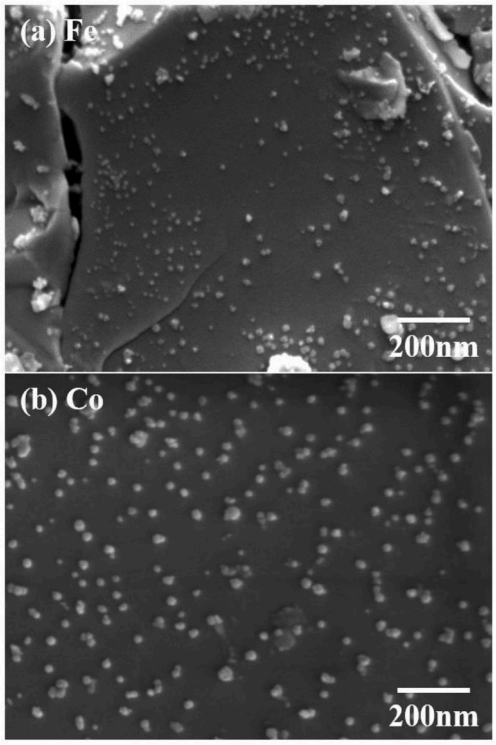

Fig. 1. SEM images of the hybrid powders of $MnSi_{1.787}Al_{0.01}$ and (a) Fe and (b) Co NPs.

simultaneously. In this study, phase analysis of the nanocomposites was performed by XRD measurements as shown in Fig. S1. The patterns of the nanocomposites resemble that of the $Mn_{15}Si_{26}$ matrix. The metal NP phase is not detected in the XRD pattern owing to the small amounts of metals. To investigate the effect of NPs on the chemical bonding of the $MnSi_{1.787}Al_{0.01}$ matrix, XPS of the Mn and Si 2*p* core levels of the $MnSi_{1.787}Al_{0.01}$ matrix and nanocomposites were measured (Figs. S2 and S3). The peaks of the Mn and Si 2*p* core levels for the nanocomposites were not shifted compared to those of the $MnSi_{1.787}Al_{0.01}$ matrix, indicating that Fe and Co NPs did not affect the chemical bonding of the $MnSi_{1.787}Al_{0.01}$ matrix [19,24]. FE-SEM images in Fig. 1 clearly confirm that the NPs (Fe and Co) are decorated on the surface of $MnSi_{1.787}Al_{0.01}$ powders, and their sizes range from 5 to 15 nm for Fe and 10–30 nm for Co. Despite the same experimental conditions for the decoration of NPs, the difference in size between the Fe and Co NPs was caused by the differences in thermal decomposition temperature, diffusion rate, and wettability between the HMS surface and the corresponding NPs [25].

HRTEM, SAED, low-magnification TEM, and EDS images are presented in Fig. 2 and Fig. S4, confirming the size and distribution of the metal NPs in 0.6 vol% Fe NP-embedded nanocomposites after the SPS process. We carried out TEM/EDS analysis at several areas to observe the location and size of the NPs and the interfaces between the matrix and Fe NPs. The HRTEM image in Fig. 2 (a) shows parallel lattice fringes with the corresponding SAED pattern along the [120] zone axis as shown in the inset. The low-magnification TEM images of the SPSed nanocomposite in Fig. 2(b) and Fig. S4 (a) highlight the grain boundaries of the nanocomposite with numerous nanopores and NPs that are located randomly near the grain boundaries with a size of approximately 50–100 nm. The change in sizes of Fe NPs is caused by the diffusion and growth process during the SPS process. To minimize the growth of NPs after the SPS process, the duration of SPS was kept as short as possible. To determine the elemental composition of the NPs, EDS analysis was performed as shown in Fig. 2 (c)–(f) and Fig. S4 (b)–(e). The results of the EDS analysis clearly indicate that the particles near the grain boundary are Fe NPs, thereby indicating that Fe did not form a compound with the elements in the $MnSi_{1.787}Al_{0.01}$ matrix.

3.2. *Electronic transport properties of Fe and Co NP-embedded nanocomposites*

The temperature dependences of σ and S of the nanocomposites were evaluated to investigate the effects of the Fe and Co metal NPs on the electronic transport properties (Fig. 3). The σ values of all nanocomposites were higher than that of the pristine sample ($MnSi_{1.787}Al_{0.01}$) over the entire range of measured temperatures. To clarify this, we measured the n_H and μ_{Hall} by estimating a one-band model as represented in Table 1. The n_H values of the nanocomposites ($1.37–1.50 \times 10^{21}$ cm^{-3}) were higher than that of the pristine sample (1.27×10^{21} cm^{-3}), whereas the μ_{Hall} values of the nanocomposites (2.37–2.59 $cm^2\ V^{-1}\ s^{-1}$) are similar to that of the pristine sample (2.60 $cm^2\ V^{-1}\ s^{-1}$). The error range of n_H and μ_{Hall} values were investigated

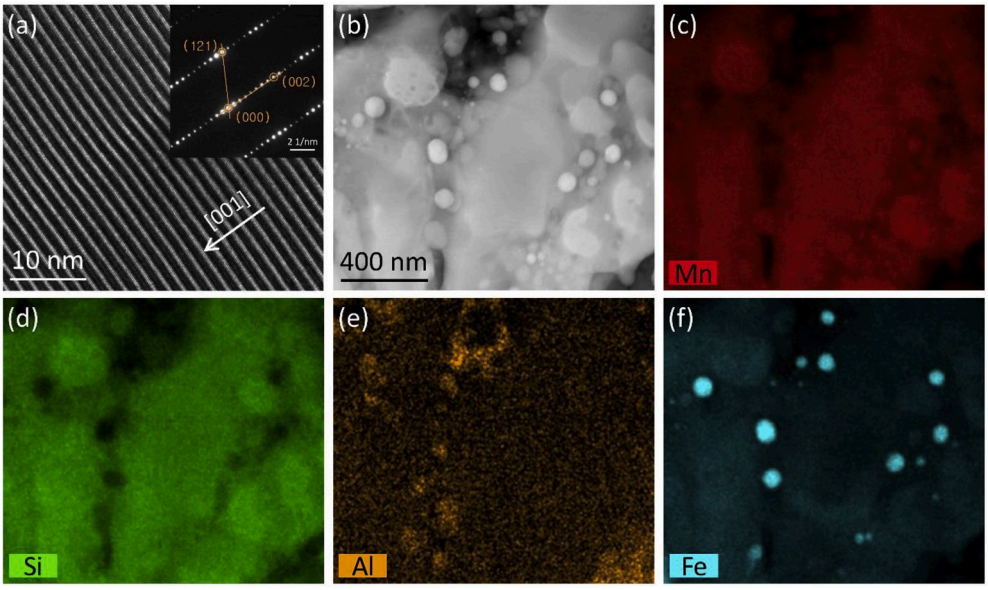

Fig. 2. (a) HRTEM, (b) low-magnification TEM images, and (c)–(f) EDS analysis of the Fe NPs-embedded nanocomposites. The inset in (a) shows the SAED pattern of the $MnSi_{1.787}Al_{0.01}$.

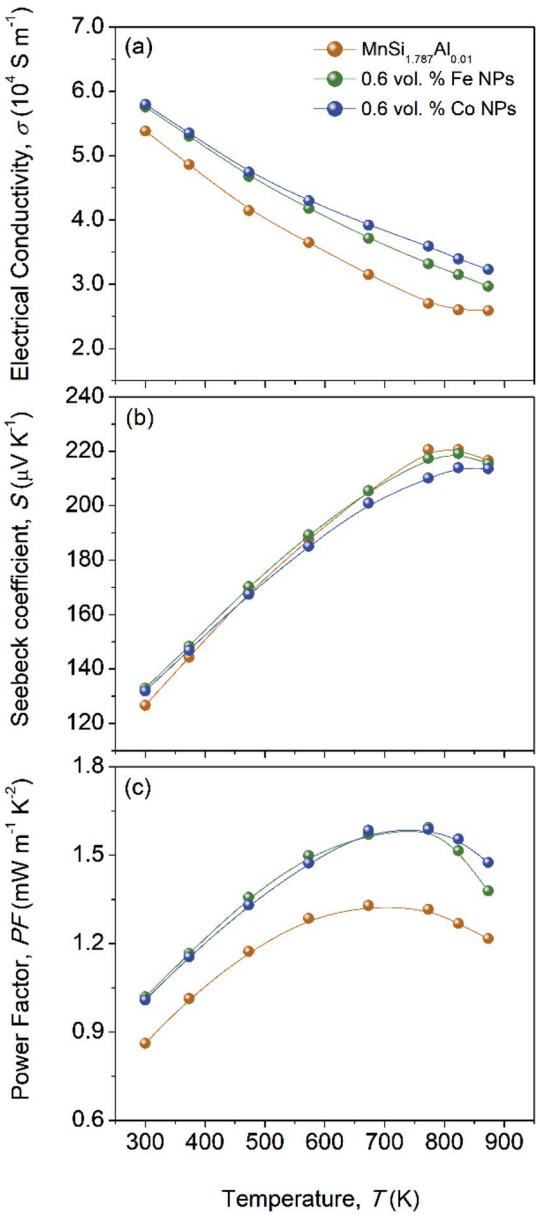

Fig. 3. Temperature dependences of (a) electrical conductivity, (b) Seebeck coefficient, (c) power factor of the metal NPs-embedded nanocomposites.

Table 1
Room temperature electronic transport parameters for the metal NPs embedded-nanocomposites.

	σ (S m^{-1})	S (μV K^{-1})	n_H (10^{21} cm^{-3})	μ_{Hall} (cm^2 V^{-1} s^{-1})
$MnSi_{1.787}Al_{0.01}$	53838.56	126.60	1.27 ± 0.25	2.60 ± 0.42
$MnSi_{1.787}Al_{0.01}$ + 0.6 vol % Fe	57601.15	133.04	1.37 ± 0.34	2.59 ± 0.52
$MnSi_{1.787}Al_{0.01}$ + 0.6 vol % Co	57968.71	131.94	1.50 ± 0.48	2.37 ± 0.57

through the repeated measuring. Though the error range were found to be about ~25% due to the small Hall voltage, it should be noted that the values of n_H and μ_{Hall} values shows clear tendency in the whole samples in this study as shown in Table 1. To confirm the differences in the electronic transport parameters, we investigated the band alignment behavior by comparing the work functions of $MnSi_{1.787}Al_{0.01}$ matrix and metal NPs that were determined using equations (1) and (2):

$$\phi = h\nu - E_{cut-off}, \quad (1)$$

where $h\nu$ is the photon energy, and $E_{cut\text{-}off}$ is the binding energy of the cut-off. The work function of $MnSi_{1.787}Al_{0.01}$ (ϕ) was estimated to be approximately 4.78 eV using UPS (Fig. 4 (a)). The work function of the metal NPs (ϕ_m) was calculated using the following equation by assuming the metal particles to be spherical [26]:

$$\phi_m(R) = \phi_\infty + \frac{5.40}{R}, \quad (2)$$

where ϕ_∞ is the work function of the bulk metals, and R is the radius of the particles (Å). The values of ϕ_{Fe} and ϕ_{Co} for Fe and Co NPs, respectively, were estimated to be in ranges 4.84–4.88 eV and 5.02–5.04 eV, respectively. From these results, we can obtain a schematic of the band structure at the interface of the $MnSi_{1.787}Al_{0.01}$ matrix and metal NPs (Fig. 4(b)). In Fig. 4 (c), the work function of metal NPs is higher than that of the $MnSi_{1.787}Al_{0.01}$ matrix. The difference between the work functions of $MnSi_{1.787}Al_{0.01}$ matrix and metal NPs leads to an ohmic contact at the interface, thereby leading to an increase in σ. Moreover, charge (e^-) transfer from the $MnSi_{1.787}Al_{0.01}$ matrix to the metal NPs also contributes to the electrical transport of the nanocomposites according to the metal-semiconductor contact theory [19]. The charge transfer effect causes an increase in n_H and σ values of the nanocomposites according to $\sigma = en_H\mu_H$. However, the significant difference between their work functions may decreases the μ_{Hall} value owing to the intensified carrier scattering at the interface between the $MnSi_{1.787}Al_{0.01}$ matrix and metal NPs.

As shown in Fig. 3(b), the S value of the nanocomposites is positive, which indicates that the major charge carriers are holes. The values of S are slightly increased in the temperature range 300–473 K. This slight increase is due to scattering of the low energy electronic carriers at the interface between the $MnSi_{1.787}Al_{0.01}$ matrix and metal NPs with band bending (Fig. 4(c) and (d)) [27]. Moreover, the multiple scattering induced by the randomly turned magnetic moment from superparamagnetism of the Fe and Co NPs affects the electronic transport properties, especially S values [19]. The magnetic properties of the nanocomposites are shown in Fig. S5. The $MnSi_{1.787}Al_{0.01}$ exhibited paramagnetism at room temperature. However, the Fe NP-embedded nanocomposite has superparamagnetism due to the low blocking temperature (295 K) [19]. The integrated scattering, induced by band bending and superparamagnetism of NPs caused the maintaining S values due to the energy filtering effect despite the manifestation of the charge transfer effect. It was found that the offset effect between the charge transfer and energy filtering effect resulted in increased n_H values in the magnetic NP-embedded nanocomposites as shown in Table 1. However, an unexpected abnormal temperature dependence caused a decrease in S values at high temperature. This result reveals that the band alignment should be precisely controlled to obtain enhanced σ and S values simultaneously. It should be noted that the power factor of the 0.6 vol% Fe and Co NP-embedded nanocomposite were significantly improved as shown in Fig. 3 (c). The power factor of 0.6 vol% Fe NP-embedded nanocomposite is enhanced by ~21% compared to that of pristine samples. This considerable increase in power factor is due to the combination effect of the charge transfer and energy filtering effects, and to realize similar band bending in related materials (p-type semiconductors) following criteria should be considered for design of materials. Most of all, introduced metal should have a higher work function than that of the matrix. Secondly, the metal should not react with the matrix. This can be controlled via engineering sintering conditions. Lastly, the metal should be in nanoscale. More details on why these conditions are necessary will be investigated in future studies.

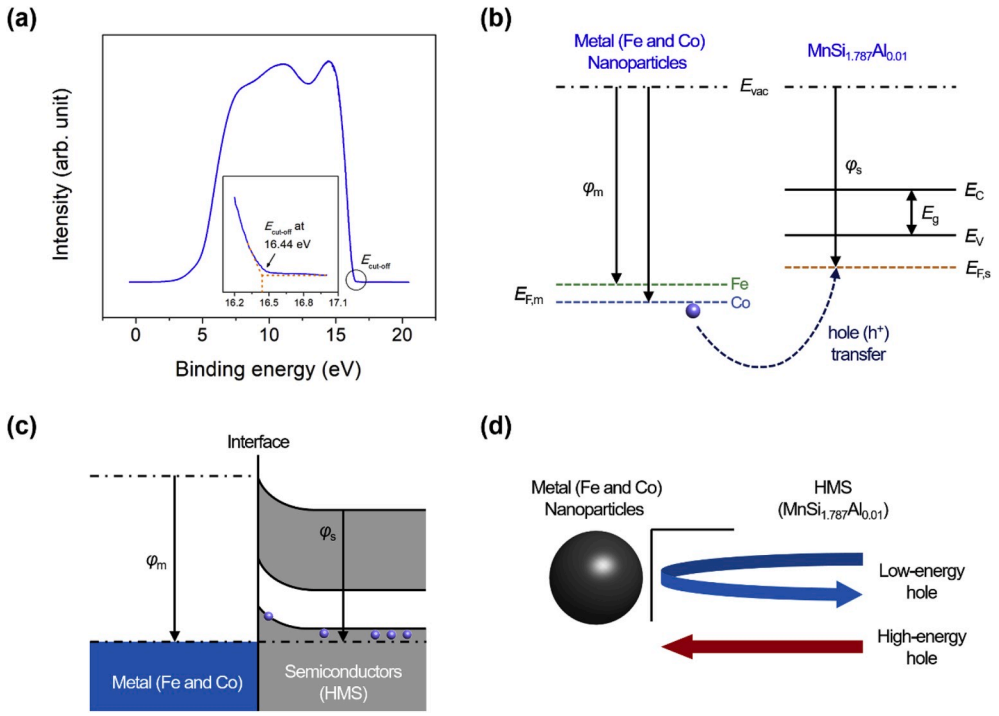

Fig. 4. (a) Ultraviolet photoemission spectroscopy (UPS) spectrum of the $MnSi_{1.787}Al_{0.01}$ matrix. (b) Schematic of the band structure of the $MnSi_{1.787}Al_{0.01}$ matrix and metal NPs. (c) Band bending induced by well-controlled band alignment. (d) Hole scattering caused by band bending at the interfaces between $MnSi_{1.787}Al_{0.01}$ matrix and metal NPs. The inset in (a) shows a close-up of the highlighted region of the spectrum.

3.3. Thermal transport properties of Fe and Co NP-embedded nanocomposites

The temperature dependences of κ_{tot} and $\kappa_{lat} + \kappa_{bp}$ values of the nanocomposites were evaluated to investigate the effect of the metal NPs on the thermal transport properties (Fig. 5(a) and (b)). The κ_{tot} of the 0.6 vol% Fe and Co NP-embedded nanocomposites (2.26–2.41 W m^{-1} K^{-1} at 373 K and 2.33–2.51 W m^{-1} K^{-1} at 773 K) were found to be similar compared to those of the pristine sample (2.41 W m^{-1} K^{-1} at 373 K and 2.40 W m^{-1} K^{-1} at 773 K). To clarify the scattering mechanism, we calculated the $\kappa_{lat} + \kappa_{bp}$ by subtracting the κ_{ele} from κ_{tot}. κ_{ele} was determined from the Wiedemann-Franz law ($\kappa_{ele} = L\sigma T$). The L was calculated using the following equation:

$$L = \left(\frac{k_B}{e}\right)^2 \left(\frac{\left(r + 7/2\right)F_{r+5/2}(\eta)}{\left(r + 3/2\right)F_{r+1/2}(\eta)} - \left[\frac{\left(r + 5/2\right)F_{r+3/2}(\eta)}{\left(r + 3/2\right)F_{r+1/2}(\eta)} \right]^2 \right), \quad (3)$$

where η is the Fermi energy, $F_n(\eta)$ is the n-th order Fermi integral, and r is the scattering parameter [28]. The L value of the pristine sample was 1.63×10^{-8} V^2 K^{-2}, and those of the nanocomposites were about 1.76×10^{-8} V^2 K^{-2}. The 0.6 vol% Fe and Co NP-embedded nanocomposites (1.91–2.06 W m^{-1} K^{-1} at 373 K and 1.88–2.02 W m^{-1} K^{-1} at 773 K) have lower $\kappa_{lat} + \kappa_{bp}$ values than that of the pristine sample (2.11 W m^{-1} K^{-1} at 373 K and 2.06 W m^{-1} K^{-1} at 773 K). This indicates that there is intensified phonon scattering by the introduction of Fe and Co NPs. In a previous report, κ_{lat} was significantly decreased due to multiple phonon scattering, induced by a randomly turned magnetic domain [19]. Above the blocking temperature, the magnetic domain was randomly turned due to the magnetic transition from the ferromagnetic state to the superparamagnetic state. To clarify this effect, the Debye-Callaway model (phonon group velocity being constant) was employed to compute the κ_{lat} [29]:

$$\kappa_{lat} = \frac{k_B}{2\pi^2 v}\left(\frac{k_B T}{\hbar}\right)^3 \int_0^{\theta_a/T} \frac{\tau_{total}(z)\ z^4 e^z}{(e^z - 1)^2} dz, \quad (4)$$

where θ_a, z, k_B, v, and $\tau_{total}(z)$ are the Debye temperature, $\hbar\omega/k_B T$, Boltzmann constant, sound velocity, and the total relaxation time, respectively. The total relaxation time for each sample was calculated according to Matthiessen's rule:

$$\tau_{total}(z)^{-1} = \sum_i \tau_i(z)^{-1}, \quad (5)$$

The τ_i values in Equation (5) represent individual relaxation times corresponding to different phonon scattering mechanisms. For instance, in order to estimate the κ_{lat} of the pristine $MnSi_{1.787}Al_{0.01}$, the τ_i for the Umklapp scattering, point-defect scattering, and boundary scattering were considered (Table 2). The reciprocal of the Umklapp phonon scattering relaxation time (τ_U^{-1}) is expressed as [29]:

$$\tau_U^{-1} = A_N \frac{2}{(6\pi^2)^{1/3}} \frac{k_B V^{1/3}}{M v^3} \gamma^2 \omega^2 T, \quad (6)$$

where A_N, V, M, γ, and ω are the adjustable parameter, atomic volume, average atomic mass, Grüneisen parameter, and the angular frequency of the phonon, respectively. The A_N is required to take momentum-conserving normal phonon scattering into account. All the parameters in Equation (6) (except the A_N) are from former studies on $MnSi_{1.8}$ (the literature on $MnSi_{1.787}Al_{0.01}$ was scarce).

The reciprocal of the point-defect scattering relaxation time (τ_{PD}^{-1}) is given by Ref. [29]:

$$\tau_{PD}^{-1} = \frac{V\omega^4}{4\pi v^3}\Gamma, \quad (7)$$

The Γ is the fitting parameter describing the size and mass contrasts (origin of point-defect scattering) between $MnSi_{1.8}$ and $MnAl_{1.8}$ in Mn $(Al_{0.0056}Si_{0.9944})_{1.797}$ (=$MnSi_{1.787}Al_{0.01}$), respectively. Γ = 0.02 for $MnSi_{1.787}Al_{0.01}$ was acquired via fitting of the theoretical κ_{lat} to

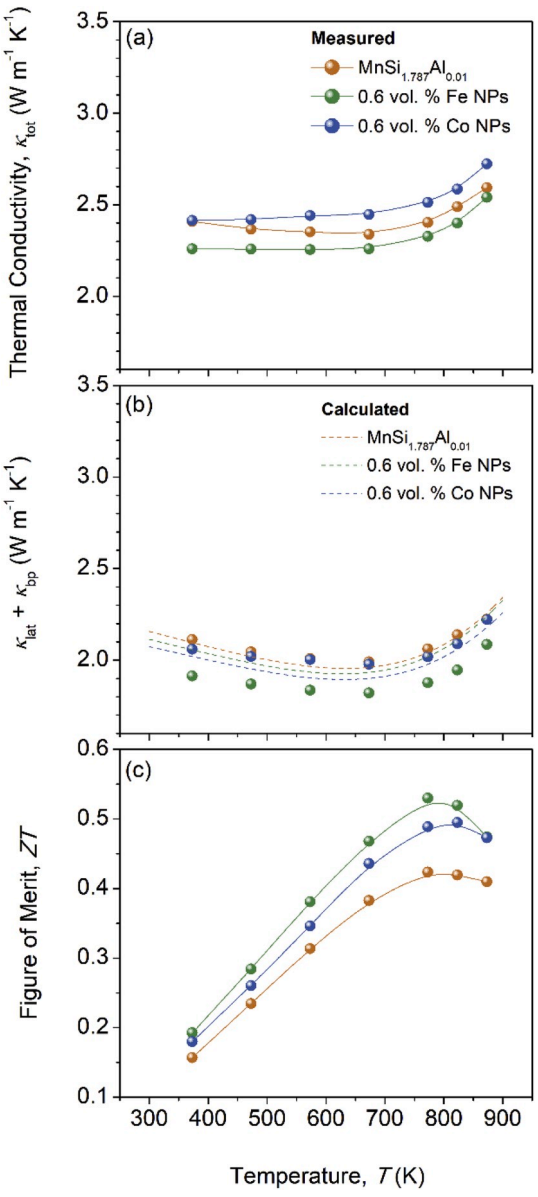

Fig. 5. Temperature dependences of (a) total thermal conductivity, (b) κ_{lat} + κ_{bp}, and (c) *ZT* of the metal NPs-embedded nanocomposites.

measured literature data from Luo [30] and Chen [13]. This is only about 14% of the Γ acquired from $(Bi_{0.25}Sb_{0.75})_2Te_3$ alloy [31]. As the Γ depends on $x(1–x)$, where x is the composition of the one of the members of the alloy, the $MnSi_{1.787}Al_{0.01}$, where 0.56% of the $MnAl_{1.8}$ is alloyed with 99.44% of $MnSi_{1.8}$, must have a very low $x(1–x)$ value because of the low level of $MnAl_{1.8}$ in the alloy.

The reciprocal of the boundary scattering relaxation time (τ_B^{-1}) is [32]:

$$\tau_B^{-1} = \frac{v}{d}, \tag{8}$$

here, d is the size of the grain. Because the average grain size of the $MnSi_{1.787}Al_{0.01}$ was observed to be 10 μm (Fig. S6), this was plugged into Equation (8) to calculate the τ_B^{-1}.

For the theoretical κ_{lat} of 0.6 vol% Fe and Co NP-embedded nanocomposites, the same τ_i values for the Umklapp, point-defect, and boundary scattering obtained from pristine $MnSi_{1.787}Al_{0.01}$ could be adopted, as the composition and the size of the grain were kept constant even after embedding the NPs. Because we could observe the Fe and Co NPs on the surface of the $MnSi_{1.787}Al_{0.01}$ grains (Fig. 1), we anticipated that they would scatter phonons via NP scattering, but not by point-defect scattering [33]. When a NP is present on a surface of a material, the reciprocal of NP scattering relaxation time (τ_{NP}^{-1}) is:

$$\tau_{NP}^{-1} = v\left(2\pi R^2\right) V_{NP}, \tag{9}$$

where R and V_{NP} are the average NP radius and the density of the NPs, respectively. For simplicity, we have hypothesized that the wavelength of the phonons is shorter than the R. This is a plausible assumption because at temperatures higher than 800 K (where the peak *ZT* of 0.6 vol % Fe NP-embedded nanocomposite occurs), its phonon wavelength reduces substantially. Based on the measured average NP radius (Fe: 5 nm and Co: 10 nm), ideal V_{NP} values were calculated for the Fe and Co NPs. The τ_i parameters considered and used (fitted and calculated) to estimate the κ_{lat} of each sample are listed in Table 2.

The κ_{bp} of each sample was approximated via the relation [21]:

$$\kappa_{bp} = F_{bp} T^p \exp\left(\frac{-E_g}{2k_B T}\right), \tag{10}$$

where F_{bp}, p, and E_g are the fitting parameters and the band gap, respectively. The calculated E_g value of 0.779 eV was adopted [34], and the F_{bp} of 0.1 was kept constant for all the sample. Only the p parameter was adjusted to describe the differing bipolar behavior of the samples.

The dashed lines presented in Fig. 5(b) represent theoretical "$\kappa_{lat} + \kappa_{bp}$" values of the samples. The estimated "$\kappa_{lat} + \kappa_{bp}$" of the pristine and the 0.6 vol% Co NP-embedded nanocomposite closely follow the experimental data. However, that of the 0.6 vol% Fe NP-embedded nanocomposite is about 0.1 W m^{-1} K^{-1} higher than the measured data (at 373 K). This trend persists even up to ~870 K. We believe this discrepancy between theoretical and experimental values can only be explained by the beneficial magnetic effect stemming from the magnetic Fe NP. Although Co is also a magnetic particle, it seems the magnetic effect in the κ_{lat} reduction is more pronounced in Fe NP-embedded nanocomposite. Therefore, the κ_{lat} values of the Fe and Co NP-embedded nanocomposites were reduced due to the synergetic effect of the increase in interface density and multiple scattering from Fe and Co NPs.

3.4. Thermoelectric figure of merit in nanocomposites

The *ZT*s of the nanocomposites are shown in Fig. 5(c). The *ZT* values of the 0.6 vol% Fe NP-embedded nanocomposite were significantly

Table 2
Total relaxation rate (τ_{total}^{-1}) and adjustable/calculated parameters used to estimate κ_{lat} of pristine ($MnSi_{1.787}Al_{0.01}$), 0.6 vol% Fe NPs-embedded nanocomposite, and 0.6 vol% Co NPs-embedded nanocomposite.

Sample	τ_{total}^{-1}	A_N	Γ	d (μm)	R (nm)	V_{NP} (m^{-3})
Pristine	$\tau_U^{-1} + \tau_{PD}^{-1} + \tau_{B(d=10\ \mu m)}^{-1}$	0.45	0.02	10	–	–
0.6 vol % Fe NP	$\tau_U^{-1} + \tau_{PD}^{-1} + \tau_{B(d=10\ \mu m)}^{-1} + \tau_{NP}^{-1}$	0.45	0.02	10	5	1.15×10^{21}
0.6 vol % Co NP	$\tau_U^{-1} + \tau_{PD}^{-1} + \tau_{B(d=10\ \mu m)}^{-1} + \tau_{NP}^{-1}$	0.45	0.02	10	10	1.43×10^{20}

improved in the whole measured temperature range primarily due to reduced thermal conductivity and an enhanced power factor. A maximum *ZT* of 0.53 was achieved at 773 K for the 0.6 vol% Fe NP-embedded nanocomposite, which is 25% higher than that of the pristine sample. Moreover, this result showed the higher TE performance than other HMS nanocomposites, as shown in Fig. S7. In the case of the 0.6 vol% Co NP-embedded nanocomposite, although the total thermal conductivity is higher than that of the pristine sample, the *ZT* values was increased by the enhanced power factor. This reveals that precise control of the band alignment is an effective route to enhance TE properties for HMS through the embedding of magnetic metal NPs.

4. Conclusions

We investigated the thermoelectric properties of soft-magnet transition-metal (Fe and Co) NP-embedded nanocomposites. The power factor of the Fe and Co NP-embedded nanocomposites increased by 21% in comparison with that of the pristine sample owing to the synergetic effects of charge transfer and energy filtering. Moreover, the lattice thermal conductivity of these nanocomposites decreased because of intensified phonon scattering due to increased interface density and multiple scattering. The maximum *ZT* of 0.6 vol% Fe NP-embedded nanocomposite was estimated to be ~0.53 at 773 K. Our result clearly reveals that precise control of band engineering is required to improve the thermoelectric properties of HMS.

Declaration of competing interest

The authors declare that they have no known competing financial interests or personal relationships that could have appeared to influence the work reported in this paper.

CRediT authorship contribution statement

Gwansik Kim: Conceptualization, Investigation, Writing - original draft. **Hyun-Sik Kim:** Methodology, Formal analysis, Writing - review & editing. **Ho Seong Lee:** Formal analysis. **Jeongmin Kim:** Formal analysis. **Kyu Hyoung Lee:** Conceptualization. **Jong Wook Roh:** Methodology, Writing - review & editing. **Wooyoung Lee:** Supervision, Writing - review & editing.

Acknowledgements

This work was supported by the National Research Foundation of Korea (NRF) grant funded by the Korea government (MSIT, 2017R1A2A1A17069528).

Appendix A. Supplementary data

Supplementary data to this article can be found online at https://doi.org/10.1016/j.nanoen.2020.104698.

References

[1] G.J. Snyder, E.S. Toberer, Complex thermoelectric materials, Nat. Mater. 7 (2008) 105–114.
[2] K. Biswas, J. He, I.D. Blum, C.I. Wu, T.P. Hogan, D.N. Seidman, V.P. Dravid, M. G. Kanatzidis, High-performance bulk thermoelectrics with all-scale hierarchical architectures, Nature 489 (2012) 414–418.
[3] X. Shi, J. Yang, J.R. Salvador, M. Chi, J.Y. Cho, H. Wang, S. Bai, J. Yang, W. Zhang, L. Chen, Multiple-filled Skutterudites: high thermoelectric figure of merit through separately optimizing electrical and thermal transports, J. Am. Chem. Soc. 133 (2011) 7837–7846.
[4] S. Chen, K.C. Lukas, W. Liu, C.P. Opeil, G. Chen, Z. Ren, Effect of Hf concentration on thermoelectric properties of nanostructured N-type half-heusler materials $Hf_xZr_{1-x}NiSn_{0.99}Sb_{0.01}$, Adv. Funct. Mater. 3 (2013) 1210–1214.
[5] L.D. Zhao, S.H. Lo, Y. Zhang, H. Sun, G. Tan, C. Uher, C. Wolverton, V.P. Dravid, M. G. Kanatzidis, Ultralow thermal conductivity and high thermoelectric figure of merit in SnSe crystals, Nature 508 (2014) 373–377.
[6] W. Liu, X. Tan, K. Yin, H. Liu, X. Tang, J. Shi, Q. Zhang, C. Uher, Convergence of conduction bands as a means of enhancing thermoelectric performance of n-type $MgSi_{1-x}Sn_x$ solid solutions, Phys. Rev. Lett. 108 (2012), 166601.
[7] X. Chen, S.N. Girard, F. Meng, E.L. Curzio, S. Jin, J.B. Goodenough, J. Zhou, L. Shi, Approaching the minimum thermal conductivity in rhenium-substituted higher manganese silicides, Adv. Energy Mater. 4 (2014), 1400452.
[8] Y. Kikuchi, T. Nakajo, K. Hayashi, Y. Miyazaki, High temperature X-ray diffraction study on incommensurate composite crystal MnSiγ – (3+1)-dimensional superspace approach, J. Alloys Compd. 616 (2014) 263–267.
[9] M. Imai, Y. Isoda, H. Udono, Thermal expansion of semiconducting silicides β-$FeSi_2$ and Mg_2Si, Intermetallics 66 (2015) 127–132.
[10] Y. Gelbstein, J. Tunbridge, R. Dixon, M.J. Reece, H. Ning, R. Gilchrist, R. Summers, I. Agote, M.A. Lagos, K. Simpson, C. Rouaud, P. Feulner, S. Rivera, R. Torrecillas, M. Husband, J. Crossley, I. Rombinson, Physical, mechanical, and structural properties of highly efficient nanostructured *n*- and *p*-silicides for practical thermoelectric applications, J. Electron. Mater. 43 (2014) 1703–1711.
[11] W.D. Liu, Z.G. Chen, J. Zou, Eco-friendly higher manganese silicide thermoelectric materials: progress and future challenges, Adv. Energy Mater. 8 (2018), 1800056.
[12] D.B. Migas, V.L. Shaposhnikov, A.B. Filonov, V.E. Borisenko, *Ab initio* study of the band structures of different phases of higher manganese silicides, Phys. Rev. B 77 (2008), 075205.
[13] X. Chen, A. Weathers, D. Salta, L. Zhang, J. Zhou, J.B. Goodenough, L. Shi, Effects of (Al,Ge) double doping on the thermoelectric properties of higher manganese silicides, J. Appl. Phys. 114 (2013), 173705.
[14] T. Itoh, S. Uebayashi, Cobalt and iron doping effects on thermoelectric properties of higher manganese silicides prepared by mechanical milling and pulse discharge sintering, J. Jpn. Soc. Powder Powder Metall. 63 (2016) 491–496.
[15] W. Luo, H. Li, Y. Yan, Z. Lin, X. Tang, Q. Zhang, C. Uher, Rapid synthesis of high thermoelectric performance higher manganese silicide with *in-situ* formed nano-phase of MnSi, Intermetallics 19 (2011) 404–408.
[16] M. Saleemi, A. Famengo, S. Fiameni, S. Boldrini, S. Battiston, M. Johnsson, M. Muhammeda, M.S. Toprak, Thermoelectric performance of higher manganese silicide nanocomposites, J. Alloys Compd. 619 (2015) 31–37.
[17] P. Norouzzadeh, Z. Zamanipour, J.S. Krasinski, D. Vashaee, The effect of nanostructuring on thermoelectric transport properties of *p*-type higher manganese silicide $MnSi_{1.73}$, J. Appl. Phys. 112 (2012), 124308.
[18] S.A. Barczak, R.A. Downie, S.R. Popuri, R. Decourt, M. Pollet, J.W.G. Bos, Thermoelectric properties of Fe and Al double substituted $MnSi_\gamma$ (γ=1.73), J. Solid State Chem. 227 (2015) 55–59.
[19] W. Zhao, Z. Liu, Z. Sun, Q. Zhang, P. Wei, X. Mu, H. Zhou, C. Li, S. Ma, D. He, P. Ji, W. Zhu, X. Nie, X. Su, X. Tang, B. Shen, X. Dong, J. Yang, Y. Liu, J. Shi, Superparamagnetic enhancement of thermoelectric performance, Nature 549 (2017) 247–251.
[20] H. Lee, G. Kim, B. Lee, K.H. Lee, W. Lee, Phase formation and thermoelectric properties of doped higher manganese silicides ($Mn_{15}Si_{26}$), J. Electron. Mater. 46 (2017) 3242–3248.
[21] H. Lee, G. Kim, B. Lee, J. Kim, S.M. Choi, K.H. Lee, W. Lee, Effect of Si content on the thermoelectric transport properties of Ge-doped higher manganese silicides, Scripta Mater. 135 (2017) 72–75.
[22] Y. Xiao, H. Wu, J. Cui, D. Wang, L. Fu, Y. Zhang, Y. Chen, J. He, S.J. Pennycook, L. D. Zhao, Realizing high performance n-type PbTe by synergistically optimizing effective mass and carrier mobility and suppressing bipolar thermal conductivity, Energy Environ. Sci. 11 (2018) 2486–2495.
[23] A.F. May, G.J. Snyder, Introduction to modeling thermoelectric transport at high temperatures, in: D.M. Rowe (Ed.), Materials, Preparation, and Characterization in Thermoelectrics, CRC Press, 2012, pp. 1–18.
[24] W. Zhao, Z. Liu, P. Wei, Q. Zhang, W. Zhu, X. Su, X. Tang, J. Yang, Y. Liu, J. Shi, Y. Chao, S. Lin, Y. Pei, Magnetoelectric interaction and transport behaviours in magnetic nanocomposite thermoelectric materials, Nat. Nanotechnol. 12 (2017) 55–60.
[25] Y. Lin, K.A. Watson, M.J. Fallbach, S. Ghose, J.G. Smith, D.M. Delozier Jr., W. Cao, R.E. Crooks, J.W. Connell, Rapid, solventless, bulk preparation of metal NP-decorated carbon nanotubes, ACS Nano 3 (2009) 871–884.
[26] D.M. Wood, Classical size dependence of the work function of small metallic spheres, Phys. Rev. Lett. 46 (1981) 749.
[27] J.P.A. Makongo, D.K. Misra, X. Zhou, A. Pant, M.R. Shabetai, X. Su, C. Uher, K. L. Stokes, P.F.P. Poudeu, Simultaneous large enhancements in thermopower and electrical conductivity of bulk nanostructured half-heusler alloys, J. Am. Chem. Soc. 133 (2011) 18843–18852.
[28] H.S. Kim, Z.M. Gibbs, Y. Tang, H. Wang, G.J. Snyder, Characterization of Lorenz number with Seebeck coefficient measurement, Apl. Mater. 3 (2015), 041506.
[29] E.S. Toberer, A. Zevalkink, G.J. Snyder, Phonon engineering through crystal chemistry, J. Mater. Chem. 21 (2011) 15843–15852.
[30] W. Luo, H. Li, F. Fu, W. Hao, X. Tang, Improved thermoelectric properties of Al-doped higher manganese silicide prepared by a rapid solidification method, J. Electron. Mater. 40 (2011) 1233–1237.

[31] S.I. Kim, K.H. Lee, H.A. Mun, H.S. Kim, S.W. Hwang, J.W. Roh, D.J. Yang, W. H. Shin, X.S. Li, Y.H. Lee, G.J. Snyder, S.W. Kim, Dense dislocation arrays embedded in grain boundaries for high-performance bulk thermoelectrics, Science 348 (2015) 109–114.
[32] H.S. Kim, S.D. Kang, Y. Tang, R. Hanus, G.J. Snyder, Dislocation strain as the mechanism of phonon scattering at grain boundaries, Mater. Horiz. 3 (2016) 234–240.
[33] J. He, S.N. Girard, M.G. Kanatzidis, V.P. Dravid, Microstructure-lattice thermal conductivity correlation in nanostructured $PbTe_{0.7}S_{0.3}$ thermoelectric materials, Adv. Funct. Mater. 20 (2010) 764–772.
[34] A. Jain, G. Hautier, S.P. Ong, C.J. Moore, C.C. Fischer, K.A. Persson, G. Ceder, Formation enthalpies by mixing GGA and GGA + *U* calculations, Phys. Rev. B 84 (2011), 045115.